14th International Symposium on Turbulence and Shear Flow Phenomena (TSFP14)
Heidelberg, Germany, July 28–31, 2026

PARTICLE CLUSTERING REGIMES WITHIN HORIZONTAL ANNULAR PIPE WITH INNER WALL ROTATION: A SENSITIZED RSM STUDY

Xiaoyu Wang, Jeanette Hussong, Suad Jakirlić
Institute of Fluid Mechanics and Aerodynamics, Technical University of Darmstadt
Peter-Grünberg-Straße 10, 64287 Darmstadt, Germany
wang.x@sla.tu-darmstadt.de, jakirlic@sla.tu-darmstadt.de

ABSTRACT

In the present study, particle clustering regimes in horizontal, particle-laden annular configurations with inner wall rotation are classified based on flow fields obtained using a multiphase Euler–Lagrange approach within an eddy-resolving, unsteady RANS computational framework. The underlying turbulence is described by a novel Reynolds stress model sensitized to account for fluctuating flow structures, in conjunction with a four-way coupled Lagrangian particle-tracking algorithm. A systematic parametric investigation is conducted to examine the influence of particle Stokes numbers and particle mass loading ratios on flow behavior under conditions of enhanced streamline curvature induced by a strong increase in rotational intensity, in combination with gravitational effects represented by the Froude number. Based on the insights gained into the structural properties of gas–particle interactions across a range of operating parameters, particle-clustering regimes can be identified that are dominated solely by gravitational or rotational forces, as well as a regime in which both effects jointly govern the flow structure.

INTRODUCTION

The understanding of particle-laden flows, particularly gas-solid flows in horizontal annular pipes, remains limited despite their broad engineering relevance. The knowledge gap is most pronounced in the context of particle interactions with turbulence, walls and other particles - effects that become increasingly significant at higher mass loadings. The restricted progress in this field is largely attributable to the lack of systematic investigations into the relative importance of the dimensionless parameters governing these flows. In addition to the flow configuration considered presently, characterized by a curvature parameter of $R_{inner}/R_{outer} = 0.5$ and Reynolds number of $Re_{D_h} = \rho_f U_{f,b} D_h/\mu_f = 8900$, the dominant control parameters include the mass loading ratio, $\Phi_m = \dot{m}_p/\dot{m}_f = 0.4$ and 1.1, which can alternatively be expressed as a volume fraction for monodispersed particle phase; the density ratio $\rho_r = \rho_p/\rho_f = 1200$, and the particle Stokes number $St = \rho_p D_p^2 U_{f,b}/(18\mu_f L) = 5.6$, 10.2 and 22.4. Here, ρ, U and $\dot{m}$ denote density, velocity and mass flux, respectively, with subscripts "f" and "p" referring to the fluid and particle phases. The horizontal annular configuration is further complicated by the combined effects of gravity and inner cylinder rotation. These are quantitatively represented by the Froude number $Fr = U_{f,b}/\sqrt{gD_h} = 8.5$ and 17 and the non-dimensional wall rotation rate $N = U_{\theta,w}/U_{f,b}$ varying with values of 0.2145, 0.429, 0.858 and 1.716, which introduce additional mechanisms that influence the flow behavior and increases its overall complexity. Recent results presented in Wang *et al.* (2025*b*) demonstrate that the eddy-resolving IIS-RSM can effectively reproduce turbulence statistics while accounting for rotationally driven destabilization. Furthermore, validations in Wang *et al.* (2025*a*) confirm that the present multiphase Eulerian-Lagrangian computational framework can reliably predict the behavior of cases characterized by high mass loadings of heavy particles. In the present study, the particle clustering regimes within horizontal particle-laden annular configurations with inner wall rotation are classified using the aforementioned turbulence model coupled with the Lagrangian particle tracking algorithm. A systematic parametric investigation is conducted to examine the effects of St, Fr, Φ_m and N on the flow behavior.

COMPUTATIONAL MODEL

Eulerian framework

The carrier fluid is assumed incompressible. Accordingly, the governing momentum equation for the velocity field within the unsteady sensitized RANS framework is expressed as:

$$\frac{\partial U_i}{\partial t} + U_j \frac{\partial U_i}{\partial x_j} = -\frac{1}{\rho}\frac{\partial p}{\partial x_i} + \frac{\partial}{\partial x_j}\left(\nu \frac{\partial U_i}{\partial x_j} - \overline{u_i' u_j'}\right) + \overline{S_m} \quad (1)$$

Here, the term $\overline{S_m}$ refers to the momentum exchange source term. It accounts for the particle-induced back-coupling force exerted on the fluid per unit mass and is calculated using the particle-source-in-cell (PSIC) method proposed by Crowe *et al.* (1977). The source term is evaluated by integrating the interaction forces F_i ($\mathbf{F_D} + \mathbf{F_G} + \mathbf{F_L}$) in Eq. (4), describing the fluid action on the particles in each computational cell:

$$\overline{S_m} = \frac{1}{\rho}\sum_i^n F_i \cdot \Delta(x - x_i) \quad (2)$$

where the effect of each particle, labeled 'i', on the fluid is localized using a Delta function at the particle's actual position. The resulting term is subsequently applied to establish the momentum coupling between the fluid and particle phases.

In the conventional RANS-RSM approach, the turbulent stress tensor $\overline{u_i' u_j'}$ represents the Reynolds stress tensor. It is obtained using a differential, near-wall, second-moment clo-

sure model underlying fully modeled turbulence (Jakirlic & Hanjalic (2002)). However, in the sensitized-RANS methodology, it corresponds to the stress tensor associated with the unresolved residual fine-scale turbulent structures (Jakirlić & Maduta (2015)). Within the framework of the latter approach, denoted as the Improved Instability-Sensitive Reynolds Stress Model (IIS-RSM), the transport equation of the specific dissipation rate, defined as $\omega^h = \varepsilon^h/k$, incorporates an additional production source term, formulated in terms of the second derivative of the underlying velocity field ($\nabla^2 U_i$). Such a formulation allows the model to adequately capture turbulence fluctuations consistent with the resolved turbulence content, in analogy with the Scale-Adaptive Simulation (SAS) concept (Menter & Egorov (2010)):

$$\left(\frac{\mathrm{D}\omega^h}{\mathrm{D}t}\right)_{IISRSM} = \left(\frac{\mathrm{D}\omega^h}{\mathrm{D}t}\right)_{RSM} + P_{IISRSM}; P_{IISRSM} = f(\nabla^2 U_i) \tag{3}$$

For brevity, the complete specification of the model is not reproduced here; comprehensive details can be found in Jakirlić & Maduta (2015) and Wang *et al.* (2025*a*).

Lagrangian particle tracking approach

The motion of particles with densities much greater than that of the carrier fluid and diameters smaller than the Kolmogorov length scale is governed by the following transport equation:

$$m_p \frac{\mathrm{d}\mathbf{u_p}}{\mathrm{d}t} = \sum \mathbf{F_i} = \mathbf{F_D} + \mathbf{F_G} + \mathbf{F_L} \tag{4}$$

where $\mathbf{F_D}$ denotes the drag force, $\mathbf{F_G}$ represents the combined action of gravitational and buoyant forces, and $\mathbf{F_L}$ corresponds to the Saffman lift force.

The particle Reynolds number is defined as:

$$Re_p = \frac{\rho_f D_p \left|\mathbf{u_f} - \mathbf{u_p}\right|}{\mu_f} \tag{5}$$

where ρ_f and μ_f are the density and the dynamic viscosity coefficient of the carried fluid, D_p is the particle diameter and $\left|\mathbf{u_f} - \mathbf{u_p}\right|$ is the magnitude of the relative slip velocity.

For a spherical particle, the drag force is expressed as:

$$\mathbf{F_D} = C_D \frac{\pi D_p^2}{8} \rho_f (\mathbf{u_f} - \mathbf{u_p}) \left|\mathbf{u_f} - \mathbf{u_p}\right| \tag{6}$$

where the drag coefficient C_D is evaluated using the empirical correlation proposed by Putnam (1961):

$$C_D = \begin{cases} \frac{24}{Re_p}\left(1 + \frac{1}{6}Re_p^{2/3}\right) & \text{if } Re_p \le 1000 \\ 0.424 & \text{if } Re_p > 1000, \end{cases} \tag{7}$$

while the combined gravitational and buoyancy forces are given by

$$\mathbf{F_G} = m_p \mathbf{g}\left(1 - \frac{\rho_f}{\rho_p}\right) \tag{8}$$

with $\mathbf{g}$ denoting the gravitational acceleration vector.

The Saffman lift force arises from local shear in the surrounding fluid, which induces a non-uniform velocity distribution along the particle surface. It is modeled using the Saffman-Mei formulation, originally developed by Saffman (1965) and subsequently extended by Mei (1992). The lift force model is based on the shear Reynolds number, defined as:

$$Re_s = \frac{\rho_f D_p^2 \left|\nabla \times \mathbf{u_f}\right|}{\mu_f}, \tag{9}$$

which is used to compute the parameters of the Saffman-Mei model:

$$\beta = \frac{1}{2}\frac{Re_s}{Re_p}, \quad \alpha = 0.3314\sqrt{\beta}, \tag{10}$$

$$f = (1-\alpha)\exp(-0.1Re_p) + \alpha. \tag{11}$$

The lift coefficient C_{LS} is approximated as

$$C_{LS} = \begin{cases} 6.46f & \text{if } Re_p < 40 \\ 6.46 \cdot 0.0524\sqrt{\beta Re_p} & \text{if } Re_p \ge 40, \end{cases} \tag{12}$$

from which the non-dimensional lift coefficient C_L is obtained as

$$C_L = \frac{3}{2\pi\sqrt{Re_s}} C_{LS} \tag{13}$$

Finally, the Saffman lift force acting on the particle is computed as

$$\mathbf{F_L} = C_L \rho_f \frac{\pi D_p^3}{6} \left(\mathbf{u_f} - \mathbf{u_p}\right) \times (\nabla \times \mathbf{u_f}) \tag{14}$$

In the present cases, where particle volume fractions are high and particle sedimentation and aggregation play a significant role, a four-way coupling strategy is adopted. Interactions involving both inter-particle and particle-wall collisions are effectively modeled using the spring-slider-dashpot approach proposed by Tsuji *et al.* (1992).

RESULTS AND DISCUSSION

Fig. 1 illustrates three distinct particle clustering regimes, classified according to the combination of N, St, Fr, and Φ_m. In Regime 1 (termed a gravity-dominated regime), particle concentration profiles exhibit a slight vertical asymmetry, with most particles accumulating in the lower half of the annular cross-section. This gravitational bias is reflected in the streamwise particle velocity, which increases in the upper-left region and decreases in the lower-right region. The particle streamlines in the (r–θ) plane reveal that a significant fraction of particles do not reach the upper half of the annulus, resulting in a vortex structure in the lower region that can be directly attributed to sedimentation effects. In Regime 2 (termed a gravity–rotation competitive regime), particles are distributed throughout the entire annular gap, with a region of

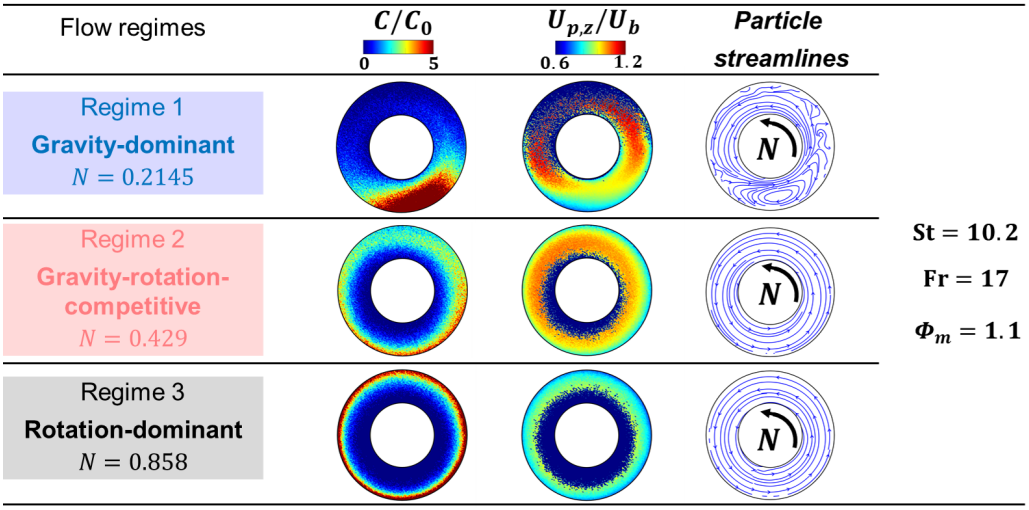

Figure 1: Particle clustering regimes classification with different rotation rates N

higher concentration located near the outer cylinder wall and predominantly in the lower half due to the continued influence of gravity. The streamwise particle velocity field tends toward axisymmetry, yet distinct left–right asymmetries emerge from the combined effects of rotation and gravity. The particle streamlines in the $(r–\theta)$ plane are nearly axisymmetric; however, particles traveling close to the inner wall collide with it in the upper half of the annulus, where insufficient momentum prevents them from overcoming gravitational forces. In Regime 3 (termed a rotation-dominated regime), centrifugal effects dominate the particle transport under the conditions of strong rotational forcing. Particles are distributed axisymmetrically along the outer cylinder wall - a pattern mirrored in the streamwise particle velocity, which becomes nearly uniform in both magnitude and spatial extent across the outer wall and the surrounding annular gap. The particle streamlines adopt concentric circular trajectories, indicating that the dynamics are governed primarily by rotation, with particles following the rotational motion of the carrier fluid.

Fig. 2 presents the particle concentration distribution normalized by its bulk-mean value C/C_0, for different parameter combinations. For cases with a low Froude number $Fr = 8.5$ and a low mass loading $\Phi_m = 0.4$, particle sedimentation consistently occurs near the bottom wall of the annulus at low rotation rates ($N = 0.2145$ and 0.429) due to gravitational settling. In contrast, as the rotation rate increases ($N = 0.858$ and 1.716), particles are redistributed throughout the entire gap, resulting in a nearly axisymmetric distribution. For higher mass loading ($\Phi_m = 1.1$), the transition between these regimes requires a higher rotation rate, with Regime 2 only occurring at $N = 1.716$. In cases with a higher Froude number ($Fr = 17$), the effect of particle mass loading is also apparent. For lower mass loading ($\Phi_m = 0.4$), particles are able to reach the upper half of the annulus even at a relative low rotation rate ($N = 0.2145$). In contrast, achieving a nearly axisymmetric particle distribution at higher mass loading ($\Phi_m = 1.1$) requires a rotation rate of at least $N = 0.429$. The influence of the Stokes number is also evident when comparing cases with $St = 5.6$ and $St = 10.2$. At $N = 0.429$ and $N = 0.2145$, it is clear that particles with a lower Stokes number ($St = 5.6$) tend to follow the behaviour of the carried fluid phase more closely, which is consistent with previous findings.

The flow regimes in Fig. 2 are identified by colored backgrounds: blue for Regime 1, pink for Regime 2, and grey for Regime 3. In Regime 1, as discussed in Fig.1, the particle phase distribution remains approximately asymmetric, indicating significant gravitational bias. The critical rotation rate, N_{crit}, represents the threshold below which particle concentration becomes asymmetric (in Regime 1). For a low Froude number ($Fr = 8.5$), the critical rotation rate is approximate $N_{crit} \approx 0.429$ for $\Phi_m = 0.4$ and $N_{crit} \approx 0.858$ for $\Phi_m = 1.1$. Additionally, for $Fr = 17$ and $\Phi_m = 1.1$, $N_{crit} \approx 0.2145$. However, even at the lowest rotation rate, Regime 1 characteristics are absent for $Fr = 17$ and $\Phi_m = 0.4$, leaving N_{crit} unknown for this parameter combination. It is also observed that N_{crit} is independent of the Stokes number within the present range ($5.6 \leq St \leq 22.4$), except in the case of $St = 5.6$ for $Fr = 8.5$ & $\Phi_m = 1.1$ and $Fr = 17$ & $\Phi_m = 1.1$, where a transition regime appears. In summary, gravitational bias is significant for low values of N and Fr.

Regime 2 is characterised by an eccentric axisymmetric distribution of particle concentration, occurring when the rotation rate exceeds the critical value ($N > N_{crit}$) for each Froude number. The occurrence of Regime 2 appears independent of St for both low and high Fr within the present scope of parameters, although there are a few transitional regimes that depends on the Stokes number. Regime 3 occurs only at relative high rotation rate ($N \geq 0.858$), where the particle distribution becomes largely axisymmetric, even under high mass loading conditions. In this regime, the rotation induced particle inertia dominants over gravitational effects, leading to a uniform particle distribution along the annular outer wall. Thus, Regime 3 could occur where the rotation rate of the inner cylinder greatly exceeds the critical value even with a lower Froude number, such as at $N = 1.716$ for $Fr = 8.5$. It should be noted that in all relevant figures, the borders between different coloured backgrounds (i.e., different flow regimes) are presented for preview purposes, and a more refined resolution of each flow parameter is required to identify qualitative distinctions between regimes.

While rotation rate appears to be the most dominant factor in distinguishing regimes, the other parameters are also significant. Although St number has less impact on the regime classification, it still affects particle concentration distribution. For all parameter combinations of Fr and Φ_m, it is clear that the extent of particle concentration shifting toward the annulus bottom enhances as the Stokes number increases, given the same rotation rate. The effects of Fr and Φ_m on regime classification are generally as expected, but these two parameters seem to

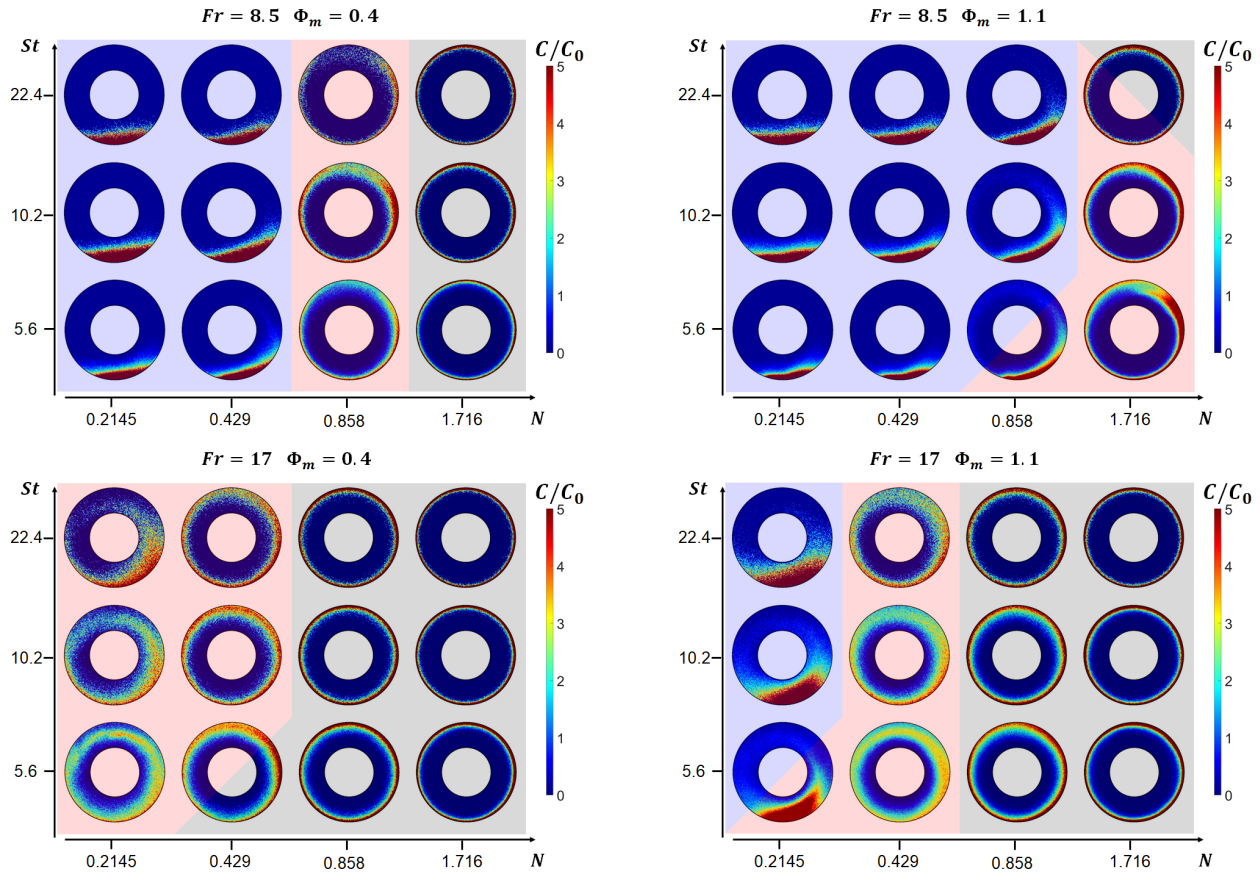

Figure 2: Color maps of the particle concentration distributions normalized by the bulk-mean value C/C_0 for a series of values of (a) $Fr = 8.5$ and $\Phi_m = 0.4$, (b) $Fr = 8.5$ and $\Phi_m = 1.1$ (c) $Fr = 17$ and $\Phi_m = 0.4$ and (d) $Fr = 17$ and $\Phi_m = 1.1$

work together. Specifically, for low rotation rates ($N \leq 0.429$) and both mass loading values ($\Phi_m = 0.4$ and 1.1), the flow corresponds to Regime 1 under low Froude number conditions ($Fr = 8.5$). However, under high Froude numbers ($Fr = 17$), for the same rotation rates $N \leq 0.429$, all cases with low mass loading ($\Phi_m = 0.4$) fall into Regime 2, while for higher mass loading ($\Phi_m = 1.1$), the flows are divided between Regime 1 and 2, depending on the rotation rates N.

The particle streamwise velocity distribution normalized by the bulk velocity of fluid $U_{p,z}/U_b$ for different parameter combinations is illustrated in Fig. 3. The streamwise velocity distributions align with the particle concentration profiles shown in Fig. 2, with non-particle regions represented by dark blue. It is evident that each flow regime exhibits distinct characteristics in term of particle streamwise velocity distributions.

In Regime 1, a clear difference in velocity magnitude is observed, with a low-velocity region near the bottom of the annulus and significantly higher velocities for particles located above this region. The contours show a transition from a low-velocity (blue) region to a moderate-velocity (green) region, and in some cases, a high-velocity (red) region appears on the right side of the annulus. This velocity distinction becomes more pronounced as the flow transitions to Regime 2, where the velocity distinction tends to be determined by left-right asymmetry rather than up-down. An exception occurs for $Fr = 8.5$ and $\Phi_m = 1.1$, where gravitational effects are more pronounced compared to other combinations of Fr and Φ_m. Hence, Regime 2 is characterised by a low-velocity region on the right side of the annulus and a high-velocity region on left side, corresponding to the areas where gravitational and rotational effects counteract and reinforce each other, respectively. In Regime 3, with further increase in the rotation rate N, the streamwise velocity distribution becomes axisymmetric near the outer cylinder wall, which reflects the dominance of rotational forces in this regime.

These distinct characteristics of the three flow regimes can be explained by different underlying mechanisms: In Regime 1, as the inner cylinder begins to rotate, particles are carried by the fluid and forced into rotation. A small number of particles, driven by centrifugal forces, leave the bottom of the annulus, become accelerated by the fluid, and exhibit higher velocities on the right side. In Regime 2, as the rotational intensity increases, most particles are lifted from the bottom and begin rotating around the center of the annulus. In this regime, gravitational and centrifugal forces create co-/counteracting effects on the left and right sides, resulting in differences in particle energy and, consequently, distinct left-right velocity distributions. In Regime 3, when the rotation rate reaches the highest value studied, particles are pushed toward the outer cylinder wall, becoming almost entirely dominated by centrifugal forces. In this region, gravity and the drag force from the carried fluid are relatively weak, leading to an axisymmetric velocity distribution. Additionally, as the rotation rate increases and the flow transitions from Regime 1 to Regime 3, the magnitude of the streamwise velocity does not change monotonically. During the transition from Regime 1 to Regime 2, the high-velocity region expands while the velocity magnitude remains nearly unchanged. However, as the flow transitions from Regime 2 to Regime 3, particle velocities are significantly reduced. A possible explanation for this deceleration is

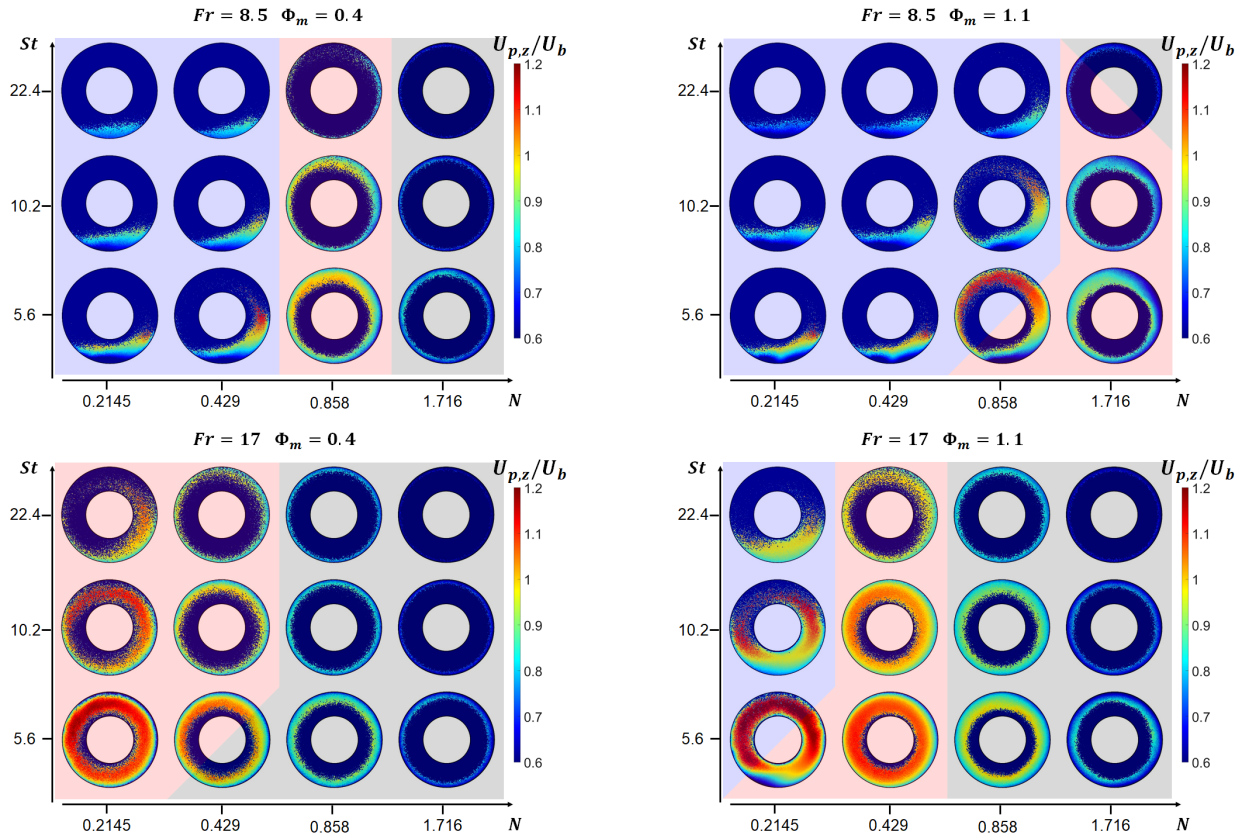

Figure 3: Color maps of the particle streamwise velocity distributions normalized by the bulk-mean value $U_{p,z}/U_b$ for a series of values of (a) $Fr = 8.5$ and $\Phi_m = 0.4$, (b) $Fr = 8.5$ and $\Phi_m = 1.1$, (c) $Fr = 17$ and $\Phi_m = 0.4$ and (d) $Fr = 17$ and $\Phi_m = 1.1$

that in Regime 3, particles are primarily located near the outer cylinder wall, where they are decelerated by the low-velocity fluid near the wall due to the no-slip boundary condition.

Furthermore, the influence of the Stokes number St is evident for all parameter combinations of Fr and Φ_m. As St decreases, the magnitude of the streamwise velocity increases for the same rotational intensity, which can be attributed to the reduced particle inertia. The effect of mass loading Φ_m is visible by comparing the left and right subplots in Fig. 3: a higher value of Φ_m leads to an increase in velocity magnitude, regardless of the flow regime. In contrast, the effect of the Froude number Fr on streamwise velocity is less straightforward; the velocity magnitude appears to be influenced by the specific flow regime rather than following a constant trend with Fr.

Fig. 4 shows the time- and space-averaged secondary flow streamlines of particles within the annular cross-section for various parameter combinations. While the rotation of the inner cylinder exerts a dominant influence on particle dynamics, each flow regime exhibits distinct structural characteristics. In Regime 1, at low rotation rates N, particles do not fully occupy the annular cross-section, leaving unpopulated regions in the upper portion of the cross-sectional area. Even when particles are more broadly distributed, their penetration into the upper region remains incomplete. A vortex structure forms near the bottom of the annulus, where particles ascend along the outer wall due to centrifugal forcing and subsequently descend under the influence of gravity. As the rotation rate N increases, the vortex core shifts in an anticlockwise direction, accompanied by an increase in vortex size. A similar transformation of the vortex is also observed with decreasing St. In Regime 2, at higher rotation rates N, the distinct vortex structure characteristic of Regime 1 disappears. Particle motion becomes increasingly dominated by centrifugal effects, resulting in trajectories that predominantly encircle the inner cylinder. The interplay of centrifugal and gravitational forces accelerates particles along the left side of the annulus while decelerating those on the right. Consequently, particle streamlines intersect the inner cylinder wall in the upper-right quadrant, where the particles' azimuthal velocity is progressively reduced due to continuous deceleration. These interactions with the inner wall are absent in Regime 3. Instead, particle streamlines form multiple concentric circles centered within the annulus, indicating that particle behavior is fully governed by the centrifugal force induced by the rotation of the inner cylinder.

CONCLUSION

For particle-laden gas-solid flow in a concentric annular configuration with a rotating inner cylinder wall, three regimes of flow behaviour have been identified that can be characterized by the parameter combination of rotation rate N, Stokes number St, mass loading Φ_m and Froude number Fr, for the case in which near-elastic collisions occur for both the particle-wall and inter-particles interactions (i.e., the coefficient of restitution are $e = 0.97$). These three regimes are as follows:

• Regime 1 (gravity-dominant) occurs for low values of N, which results in particle concentration sediment in annulus bottom and the corresponding particle streamline is not able to reach the annulus top. The particles in this regime is domi-

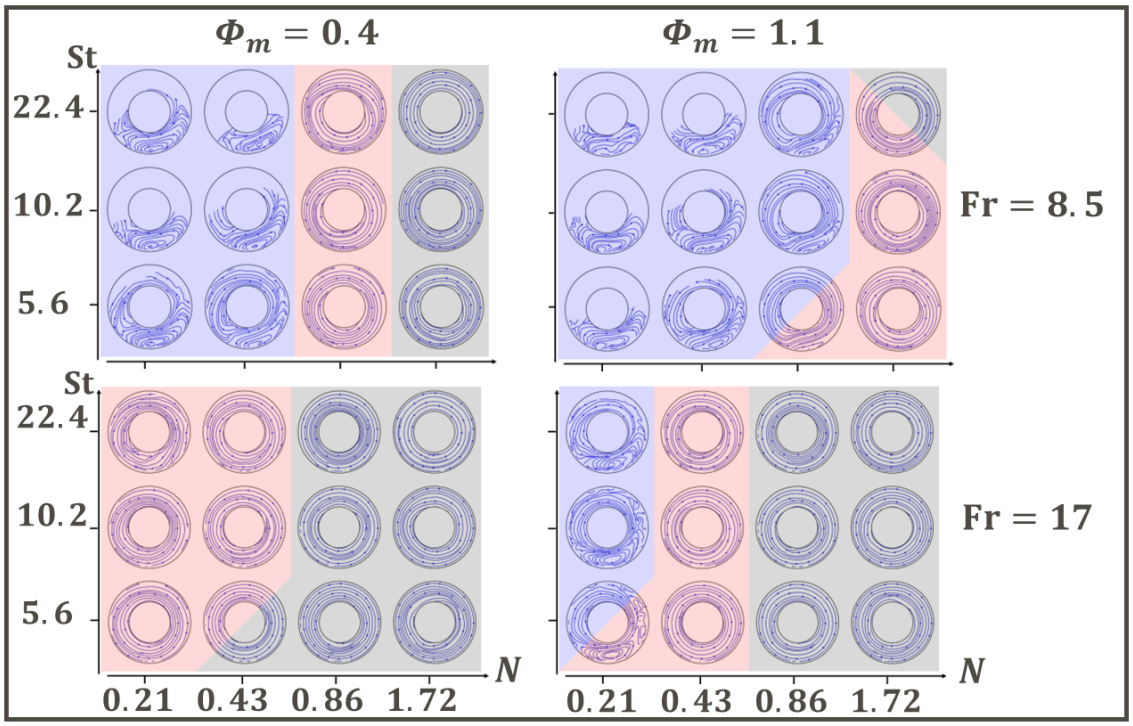

Figure 4: Particle streamlines averaged in the cut-off plane for a series of parameter combinations

nant by the gravitational bias effect. The critical value of N depends mainly on Fr and Φ_m, such that $N_{crit} \approx 0.429$ for $Fr = 8.5$ with both $\Phi_m = 0.4$ and $\Phi_m = 1.1$, $N_{crit} = 0.2145$ for $Fr = 17$ and $\Phi_m = 1.1$, N_{crit} is unknown for $Fr = 17$ and $\Phi_m = 0.4$ in the present parameter scope.

• Regime 2 (gravity-rotation-competitive) occurs when N and hence the centrifugal force is sufficiently high to lead the rotation effect to be comparable with the gravitational sediment effect. This regime represents the particles under a higher rotation rate than the critical value ($N > N_{crit}$) but below the values of N for which Regime 3 occurs.

• Regime 3 (rotation-dominant) corresponds to high value of N together with the effects of gravity being much weaker than of centrifugal force on particles, resulting in an axisymmetric distribution of particle concentration and velocity throughout the region near the outer cylinder wall. This regime was identified for the cases $N = 1.716$ for $Fr = 8.5$ and $\Phi_m = 0.4$ and $0.858 \leq N \leq 1.716$ for $Fr = 17$ in the present investigation. It can be anticipated to extend to higher rotation rates, e.g., $N > 1.716$ for $Fr = 8.5$ and $\Phi_m = 1.1$, which needs to be further confirmed.

Acknowledgements. The authors gratefully acknowledge the German Federal Ministry of Education and Research (BMBF) and the federal state of Hessen for supporting this project as part of the NHR4CES (National High Performance Computing Center for Computational Engineering Sciences) funding at Technical University of Darmstadt and RWTH Aachen and of the German Research Foundation (DFG) within the framework of the Collaborative Research Center/Transregio 150 (SFB-TRR 150, project number 237267381; https://www.trr150.tu-darmstadt.de/der_sonderforschungsbereich/ index.en.jsp). The authors furthermore acknowledge the computing time granted on the Lichtenberg HPC of the TU Darmstadt.

REFERENCES

Crowe, C. T., Sharma, M. P. & Stock, D. E. 1977 The particle-source-in cell (psi-cell) model for gas-droplet flows. *Journal of Fluids Engineering* **99** (2), 325–332.

Jakirlic, S. & Hanjalic, K. 2002 A new approach to modelling near-wall turbulence energy and stress dissipation. *Journal of Fluid Mechanics* **459**, 139–166.

Jakirlić, S. & Maduta, R. 2015 Extending the bounds of 'steady' RANS closures: Toward an instability-sensitive Reynolds stress model. *Int. J. Heat and Fluid Flow* **51**, 175–194.

Mei, R. 1992 An approximate expression for the shear lift force on a spherical particle at finite reynolds number. *Int. J. Multiphase Flow* **18** (1), 145–147.

Menter, F. & Egorov, Y. 2010 The scale-adaptive simulation method for unsteady turbulent flow predictions. part 1: Theory and model description. *Flow Turbulence and Combustion* **85**, 113–138.

Putnam, A. 1961 Integrable form of droplet coefficient. *ARS Journal* **31**, 1467–1470.

Saffman, P. G. 1965 The lift on a small sphere in a slow shear flow. *Journal of Fluid Mechanics* **22** (2), 385–400.

Tsuji, Y., Tanaka, T. & Ishida, T. 1992 Lagrangian numerical simulation of plug flow of cohesionless particles in a horizontal pipe. *Powder Technology* **71** (3), 239–250.

Wang, X., Hussong, J. & Jakirlić, S. 2025*a* Eddy-resolving Reynolds stress modeling of particle-laden flows using a multiphase Euler–Lagrange approach. *Int. J. Heat and Fluid Flow* **115**, 109853.

Wang, X., Hussong, J. & Jakirlić, S. 2025*b* Turbulence anisotropy characterization of concentric annulus flow with inner wall rotation: an eddy-resolving Reynolds stress modeling study. In *2nd European Fluid Dynamics Conference (EFDC2)*. Dublin, Ireland.